A comprehensive density functional theory study on molecular structures of (5, 5) carbon nanotube doped with B, N, Al, Si, P, Co, and Ni

Fahimeh Shojaie

Department of Photonic, Institute of Science and High Technology and Environmental Sciences, Graduate University of Advanced Technology, Kerman, Iran

ARTICLE INFO

ABSTRACT

Armchair single-walled carbon nanotubes (SWNTs), which were doped with B, N, Al, Si, P, Co, and Ni, have been studied using computational simulations based on density functional theory (DFT). The topological analysis and the electron localization function show that the nature of the interaction between carbon atoms and the dopant X atoms is not purely covalent or an ionic. In order to gain a deeper understanding of the interaction between X atoms and C atoms, calculations of natural bond orbital (NBO) analysis, bond order analysis, atomic charge analysis, and electrostatic potential (ESP) on the van der Waals (vdW) surfaces of molecules are required. The Natural population analysis (NPA), Hirshfeld and atomic dipole moment corrected Hirshfeld (ADCH) atomic charges and molecular electrostatic potential maps on vdW surfaces of $C_{79}H_{20}Xs$ show that ESP values are in good agreement with ADCH values. The calculations of The Laplacian bond order (LBO), Mayer bond order (MBO) and Fuzzy bond order (FBO) illustrate that LBO has a strong correlation with the bond length. In addition, the calculations show that Fermi energies of the pristine C (5, 5) carbon nanotubes (CNTs) and all doped CNTs are equal to the energies of their highest occupied molecular orbital (HOMO). This work presents a comparison about the bonding characteristic between the doped atoms (X) and carbon atoms.

© 2017 Published by Elsevier B.V.

1. Introduction

The discovery of CNTs by Lijima has provided opportunities to obtain a quasi-one-dimensional nanomaterial [1]. CNTs could be metallic or semi-conductive depending on their particular geometries (diameter and chirality) [2–4] and they have become the most interesting systems due to their unique structures, unusual properties and great potential for diverse applications in electronic, thermal, mechanical, biological, and chemical fields [5–13]. Pristine SWNTs can be used as sensors for the detection of gases [14–18] and proteins [19,20] and for drug delivery to body organs [21,22]. The adsorption capability of SWNTs can be improved through formation of active sites on tube walls, in order to enhance detection of gas molecules, organic chemicals and biological substances.

Doping introduces impurities into SWNTs for the purpose of enhancing their efficiency of adsorption of molecules [23–26]. Doped SWNTs are considered to be new nanotechnological materials. Several research groups have carried out experimental and theoretical studies on the effects of doping on CNTs. Dopant enhances CNTs ability to absorb gaseous molecules [27,28]. This discovery

has created immense interest on the doped SWNTs as promising materials for gas sensors. DFT calculations have shown that the boron-doped (B-doped) SWNT is a good candidate for detecting HCOH [29], toxic carbon monoxide [24], cyanide [26], NO and H_2 molecules [27]. The electronic structure of the B-doped (10, 0) CNTs has been studied by Koretsune et al. [30] Baei [31] studied the electronic structural properties of the pristine and the aluminum-doped (Al-doped) forms of (4, 4) and (6, 0) CNTs using the chemical shielding tensors at the sites of various ^{13}C and ^{27}Al nuclei. He showed that the calculated bond lengths of Al-doped armchair and zigzag models are significant compared to the calculated bond lengths of the C atom in their pristine carbon nanotubes. The DFT calculations show that the Al-doped SWNT is a good candidate for detecting carbon monoxide [32] and NH_3 [33]. Computational studies of adsorption of H_2, H_2O, O_2, CO, CO_2, NO, NO_2, NH_3, and CH_3OH molecules on the surfaces of B-doped CNT (B-CNT) and silicon-doped (Si-doped) CNT (Si-CNT) show that the B-CNT and Si-CNT adsorbent materials would be good candidates for gas sensor applications [34] such as detection of hydrogen halide gases HX (X = F, Cl, Br and I) by the electronic structures of the B-CNT and N-CNT were reported by Hizhnyi et al. [35].

Although theoretical modelling is an important technique to predict important physical and chemical properties of adsorption

E-mail address: f.shojaie@kgut.ac.ir

of molecules on the CNT surface for elaboration of novel gas sensors, no calculations have been reported on the bonding nature of the doped CNTs in the literature. A chemical bond is the result of attraction between atoms or ions. The physical properties of materials, such as melting point and electrical conductivity, are determined by the types of bonds. Bond order is used for quantitative description of chemical bonds. It is useful to understand the nature of molecular electronic structure and predict the molecular reactivity, aromaticity and stability.

The purpose of this work is to get a theoretical insight into electronic properties, the nature of the chemical bond based on the topological analysis of electron density, the natural electronic configurations by natural bond orbital analysis, the bond order analysis based on the Laplacian electron density, atomic charge analysis, and electrostatic potential on the van der Waals surfaces of $C_{79}H_{20}Xs$ using computational simulations according to density functional theory. On the other hand, these results can introduce novel and crucial information on the bonding principles of the doped atoms (X) and carbon atoms. Thus, we have studied the bonding difference between the doped atoms (X) and the carbon atoms and the covalent nature of the X—C bonds in doped SWNTs (5, 5). The nature of the interaction between doped atoms and carbon atoms have been investigated through topological analysis and it could be stated that the nature of binding between C and the X atoms is not purely covalent or ionic. A comparison between the bonding characteristics can provide detailed and novel information about the principles of X—C bonding. Such information helps us to understand the mechanism of doped SWNTs. SWNTs, doped with B, N, Al, Si, P, Co and Ni impurities, have been extensively studied. It is interesting to note that B and Al atoms have one valence electron less than carbon atom, N and P atoms have one valence electron more than carbon atom, Si atom has same number of valence electrons as carbon atom and Co and Ni atoms are first row transition elements. The chemical formulae of the SWNTs, doped with B, N, Al, Si, P, Co and Ni impurities, are: $C_{79}H_{20}B$, $C_{79}H_{20}N$, $C_{79}H_{20}Al$, $C_{79}H_{20}Si$, $C_{79}H_{20}P$, $C_{79}H_{20}Co$ and $C_{79}H_{20}Ni$. Symbol X in $C_{79}H_{20}X$ represents any of B, C, N, Al, Si, P, Co or Ni atom. $C_{79}H_{20}Xs$ is the plural form of $C_{79}H_{20}X$ and represent all the above doped SWNTs.

2. Computational modelling

The initial geometries of $C_{79}H_{20}Xs$ were optimized by Becke's three-parameter Lee-Yang-Parr hybrid functional (B3LYP) [36] with 6-31+G and 6-31G(d) basis set using Gaussian 09 program [37]. To investigate the effect of d polarization and diffuse functions on the structural properties and the bonding nature of doped SWNT atoms, 6-31+G and 6-31G(d) basis sets were used. Manzetti explained that the band gaps, produced by B3LYP/6-31G(d) functional, are quite satisfactory [38]. In addition, it has been demonstrated that a polarized basis set is necessary to predict the metallic behavior of armchair SWNTs accurately. Small displacements in the armchair SWNTs atom positions do not influence the choice of the basis set [39]. Meanwhile, there are very little differences between the initial geometries of $C_{80}H_{20}$, which were calculated by 6-31+G and 6-31G(d) basis sets. The B3LYP/6-31+G and B3LYP/6-31G(d) functionals allow short computing times.

Energies of all optimized configurations were evaluated by M06-2X density functional method [40] using 6-31+G, 6-31G(d) and SDD basis sets for comparison purposes. It is known that M06-2X is a very ideal choice for main group elements [41]. The SDD is the basis set which contains the Stuttgart/Dresden effective core potential of transition metals and the Huzinaga-Dunning double-zeta function of lighter elements [42]. The advantage of using SDD is its fast calculations with relatively better accuracy and structural modelling [43].

To determine the nature of interaction between doped atoms and carbon atoms, the topological analysis of the electron densities was performed with the help of a Multifunctional Wavefunction (Multiwfn) Analyzer [44] and the quantum theory of atoms in molecules (QTAIM). The NBOs of optimized geometries of SWNTs were calculated by Gaussian 09 using the 6-31G, 6-31G(d) and SDD basis sets. Natural population analysis (NPA) [45] and atomic dipole moment corrected Hirshfeld (ADCH) [46] charges were calculated by running the NBO module which is embedded in Gaussian and Multiwfn code. The charges, which are calculated by NPA and ADCH methods, give information about charge concentration or depletion on each atomic site. The Laplacian bond order (LBO) [47], Mayer bond order (MBO) [48] and Fuzzy bond order (FBO) [49] of the doped SWNTs have been calculated by Multiwfn code. In addition, for further confirmation of the bonding properties, the electron localization function (ELF) [50] was also calculated by Multiwfn code. Electrostatic potential (ESP) on molecular vdW surface has been calculated by Multiwfn 3.3.9 code and isosurface maps were rendered by VMD 1.9.1 program [51] based on the outputs of Multiwfn code. The structures of $C_{79}H_{20}Xs$ are presented in Fig. 1.

3. Results and discussion

3.1. Molecular orbital

The gap between the HOMO and lowest unoccupied molecular orbital (LUMO) energy levels is an important indicator of reactivity of a molecule. Table 1 indicates that values of energy gap calculated by B3LYP functional are significantly different from the energy gaps obtained by M06-2X method. Nevertheless, both sets of data show a similar trend. The energy gaps of the optimized $C_{79}H_{20}X$, which have been calculated by B3LYP and M06-2X using 6-31+G and 6-31G(d) basis sets, are nearly equal. Zhou et al. [52] reported that the calculated energy gap of $C_{80}H_{20}$ is 1.73 eV. Zhou's value is comparable to our energy gaps of optimized $C_{80}H_{20}$ which were calculated by B3LYP/6-31+G and B3LYP/6-31G(d) methods to be 1.727 eV and 1.755 eV respectively.

The energy gaps of $C_{79}H_{20}Xs$ are lower than their pristine forms. A pristine SWNT is characterized as a hard molecule based on its absolute hardness and softness parameters and therefore has a lower reactivity than its doped form. The alpha gap arises from spin up electron and beta gap arises from spin down electron in open shell systems. $C_{79}H_{20}N$ has a lower alpha energy gap than other open shell systems. The beta energy gap of $C_{79}H_{20}Al$ is lower than other open shell systems. The alpha energy gap of $C_{79}H_{20}P$ is
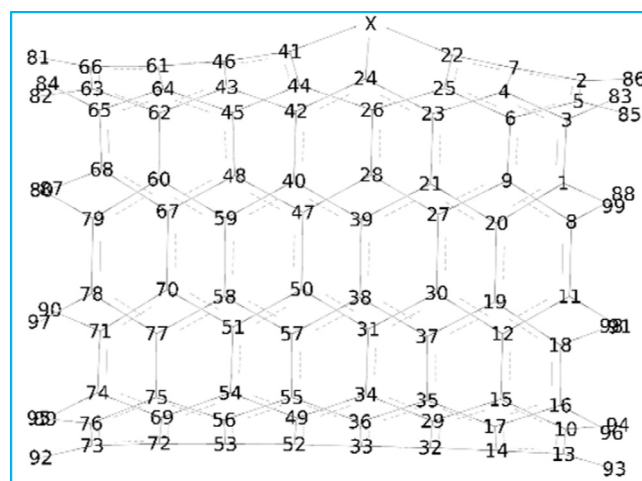

Fig. 1. The structures of $C_{79}H_{20}Xs$.

Table 1
The energy gaps of $C_{79}H_{20}Xs$.

C79H20X		B3LYP/6-31+G	M06-2X/6-31+G[a]	M06-2X/SDD[a]	B3LYP/6-31G(d)	M06-2X/6-31G(d)[b]	M06-2X/SDD[b]
X = B	Alpha	1.592	2.851	2.883	1.623	2.916	2.906
	Beta	1.379	2.600	2.609	1.356	2.631	2.617
X = C	–	1.728	3.030	3.058	1.755	3.069	3.088
X = N	Alpha	1.408	2.636	2.656	1.417	2.666	2.667
	Beta	1.591	2.861	2.894	1.621	2.901	2.919
X = Al	Alpha	1.592	2.854	2.891	1.639	2.916	2.943
	Beta	1.361	2.610	2.639	1.364	2.631	2.661
X = Si	–	1.470	2.743	2.773	1.509	2.806	2.844
X = P	Alpha	1.722	3.005	3.047	1.737	3.030	3.058
	Beta	1.518	2.774	2.813	1.516	2.786	2.826
X = Co	Alpha	1.550	2.860	2.912	1.558	2.886	2.922
	Beta	1.527	2.809	2.853	1.525	2.820	2.869
X = Ni	–	1.233	2.736	2.750	1.274	2.810	2.788

[a] These energies were obtained after B3LYP/6-31+G geometry optimization.
[b] These energies were obtained after B3LYP/6-31G(d) geometry optimization.

very close to the energy gap of its pristine form. A small energy gap leads to a large electric conductivity at a specific temperature. In general, the energy gaps of the $C_{79}H_{20}Xs$, calculated by B3LYP/6-31+G method, are smaller than their corresponding energy gaps which were calculated by B3LYP/6-31G functional.

3.2. Density of states

Density of states (DOS) spectra may help to gain a deeper understanding of the effect of dopants on the electronic properties of the pristine SWNTs. The effect of impurities on the electronic properties of SWNTs may be studied with the help of DOS. DOS of perfect and defected $C_{79}H_{20}Xs$ have been calculated and their DOS versus Hartree energy graphs have been plotted in Fig. 2. The energy levels of the HOMOs are in the range of −4.681 to −5.498 eV and the energy levels of LUMOs are in the range of −2.045 to −3.746 eV. Our calculations show that Fermi energies of all pristine SWNTs (5, 5) and doped SWNTs (5, 5) are equal to their HOMO energies.

The pristine and doped SWNTs have metallic behavior. Fig. 2 shows that the differences between the DOS of the pristine SWNTs and their doped SWNTs are very small and the trends of all SWNT DOS are essentially similar. Our results indicate that the DOS spectra of SWNTs in the valence band, calculated by M06-2X/6-31+G, M06-2X/SDD (energies optimized by B3LYP/6-31+G) and M06-2X/SDD∗ (energies optimized by B3LYP/6-31G(d)), are identical except the DOS spectra which were calculated by M06-2X/6-31G(d) method. In addition, the DOS spectra of SWNTs in valence band, which are calculated by B3LYP/6-31+G and B3LYP/6-31G(d), are approximately identical. However, the DOS spectra of SWNTs near the Fermi level, which were calculated by B3LYP/6-31+G and B3LYP/6-31G(d), are larger than the DOS spectra which were calculated by all other methods listed in this work. Fig. 2 plots shows that the trend of DOS spectra is similar to the trend of energy gap. When the band gap is very small, a SWNT resembles a metal and the electrons need less energy to transit from the valence band to the conduction band. It seems a small energy gap and the presence of a doping material can slightly increase conductivity.

3.3. Topological analysis

The bond critical point (BCP) is a saddle point in the electron density distribution, $\rho(r)$, where the gradient of the density, $\nabla\rho(r)$, vanishes i.e. $\nabla\rho(r) = 0$. The BCP is characterized by three local curvatures ($\lambda 1$, $\lambda 2$ and $\lambda 3$) that are the trace of the Hessian matrix of electron density [53]. The $\lambda 1$ and $\lambda 2$ are negative and perpendicular to the bond path ($\rho(r)$ is a maximum). The $\lambda 3$ is positive and tangential to the bond path ($\rho(r)$ is a minimum). The Laplacian of the electron density at a point, $\nabla^2\rho(r)$, is the sum of three curvatures or eigenvalues of the density at that point. Generally, electron concentration has a negative Laplacian and a positive Laplacian is associated with electron depletion. Several quantities can be evaluated at BCP, such as the kinetic energy density, $G(r)$, which is always a positive quantity, and the potential energy density, $V(r)$. The local energy density, $E(r)$, is related to the Laplacian by the following equation:

$$E(r) = 1/4\nabla^2\rho(r) - G(r) = V(r) + G(r)$$

The nature of bond interactions can be rationalized as follows: if $\nabla^2\rho(r) < 0$, $E(r) < 0E$, $\rho(r) > 0.02$, $-G(r)/V(r) < 1$ and $G(r)/\rho(r) < 1$ then the observed interaction is of covalent type and if f $\nabla^2\rho(r) > 0$, $E(r) > 0E$, $\rho(r) < 0.10$, $-G(r)/V(r) > 1$ and $G(r)/\rho(r) > 1$ then the interaction may be described as an ionic bond [54,55].

To further characterize the nature of different chemical bonds, the topological analysis of electron density of the $C_{79}H_{20}Xs$ has been performed. The AIM descriptors at the BCP for $X-C_{41}$, $X-C_{24}$ and $X-C_{22}$ bonds are given in Tables 2 and S1. Natural electronic configurations of X and C atoms in the $C_{79}H_{20}Si$ are given in Tables 3 and S3. Tables 2 and 3 show that the Laplacians of the electron density of the bonds are positive except those of N—C and P—C bonds which are negative. The local energy densities of the bonds are all negative, but densities of Al—C bonds are lower than those of other X—C bonds. The $\rho(r)$ values of Al—C are smaller than 0.10 au. The $\rho(r)$ increases from 0.091 au at Al—C BCP to 0.290 au at N—C BCP (See Table 2), suggesting that the Al—C bonds have a weaker covalent character compared to the N—C bond. All values of $-G(r)/V(r)$ lie below 1, but $-G(r)/V(r)s$ of Al—C bond are closest to 1.0. The ratio of the local kinetic energy density to the electron density is smallest for N—C and largest for Al—C. Our results show that the nature of the interaction between C and the X atoms is not purely covalent or ionic. Therefore, most of the X—C bonds can be characterized as intermediate types between covalent and ionic. The N—C bond is most covalent whereas the Al—C bond is most ionic. There are insignificant differences between the electron density descriptors of $X-C_{22}$, $X-C_{24}$ and $X-C_{41}$. However, $X-C_{24}$ bond is slightly weaker than $X-C_{22}$ and $X-C_{41}$. The electron density descriptors, which have been calculated by all our methods, are identical.
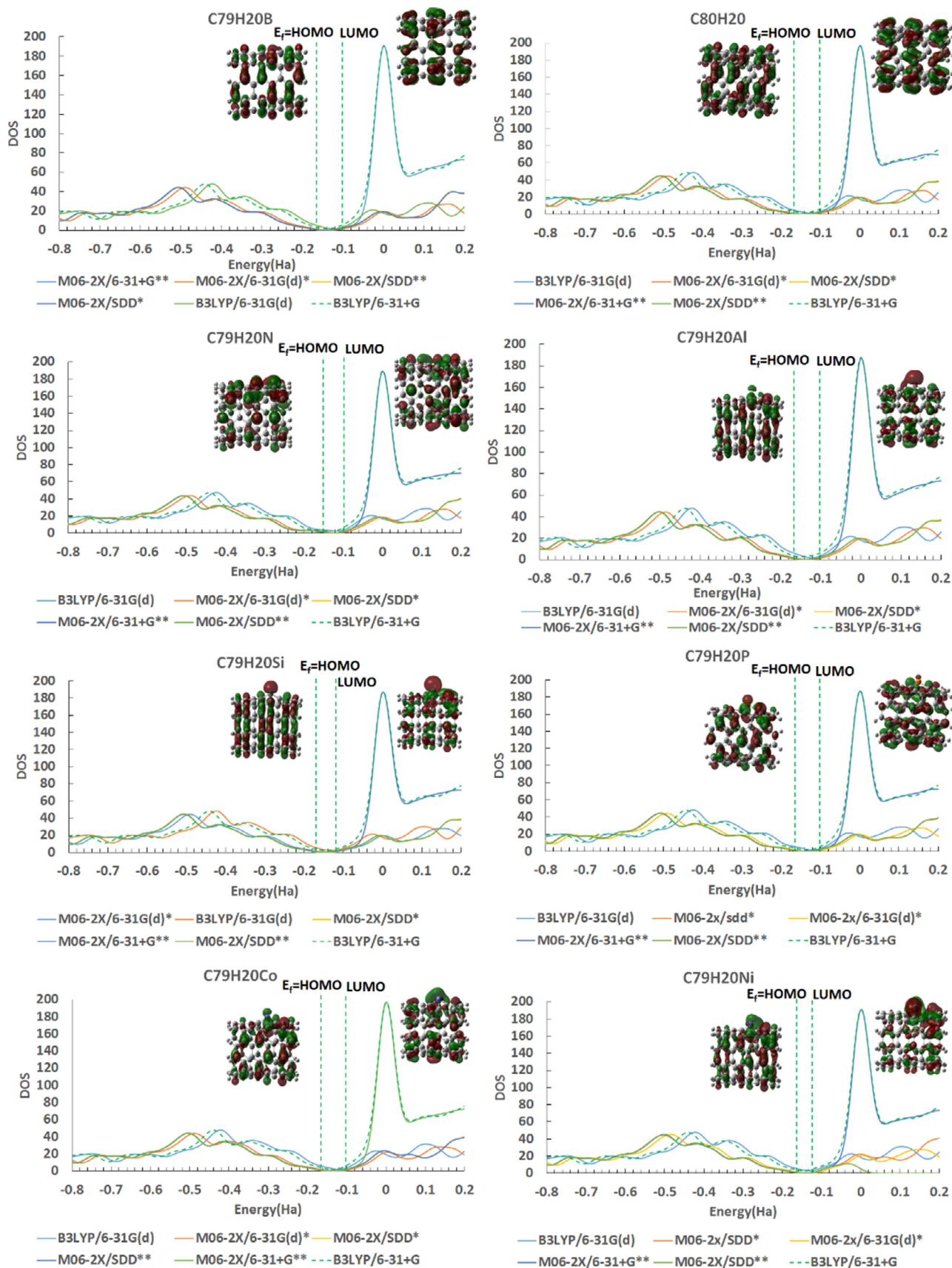
Fig. 2. DOS (Alpha) spectral plots for $C_{79}H_{20}$Xs. ** DOS of geometrically optimized $C_{79}H_{20}$X (Optimization was performed by 6-31+G method). * DOS of geometrically optimized $C_{79}H_{20}$X (Optimization was performed by 6-31G(d) method). The energy gap was calculated by B3LYP method using 6-31+G basis set.

Table 2
Electron density descriptors (au) at the bond critical points (BCP) between X and C Atoms obtained from the 6-31G(d) geometry optimization.

C79H20X	BCP	$\rho(r)$	$\nabla^2\rho(r)$	$E(r)$	$-G(r)/V(r)$	$G(r)/\rho(r)$	ε
X = B	X-C22	0.194	0.026	−0.195	0.508	1.036	0.103
	X-C24	0.189	0.047	−0.186	0.515	1.051	0.089
	X-C41	0.194	0.038	−0.195	0.512	1.049	0.102
X = N	X-C22	0.287	−0.820	−0.412	0.334	0.721	0.103
	X-C24	0.285	−0.787	−0.409	0.342	0.745	0.131
	X-C41	0.290	−0.824	−0.422	0.339	0.744	0.115
X = Al	X-C22	0.097	0.486	−0.024	0.859	1.495	0.097
	X-C24	0.091	0.433	−0.022	0.857	1.429	0.117
	X-C41	0.097	0.490	−0.024	0.860	1.502	0.098
X = Si	X-C22	0.131	0.487	−0.070	0.733	1.466	0.196
	X-C24	0.123	0.418	−0.066	0.721	1.384	0.225
	X-C41	0.129	0.462	−0.070	0.726	1.432	0.169
X = P	X-C22	0.164	−0.002	−0.157	0.499	0.955	0.185
	X-C24	0.156	−0.081	−0.150	0.464	0.827	0.202
	X-C41	0.164	0.014	−0.157	0.506	0.976	0.184
X = Co	X-C22	0.172	0.285	−0.088	0.644	0.924	0.084
	X-C24	0.158	0.270	−0.077	0.653	0.914	0.061
	X-C41	0.171	0.288	−0.087	0.647	0.926	0.076
X = Ni	X-C22	0.164	0.157	−0.101	0.581	0.859	0.099
	X-C24	0.146	0.126	−0.087	0.576	0.813	0.035
	X-C41	0.166	0.135	−0.102	0.571	0.820	0.066

Table 3
Natural electronic configurations of X and C atoms in the $C_{79}H_{20}X$ systems obtained from the B3LYP/6-31G(d) geometry optimization.

X		X	C22	C24	C41
X = B	Alpha	$[He]2S^{(0.28)}2p^{(0.92)}$	$[He]2S^{(0.47)}2p^{(1.66)}3p^{(0.01)}$	$[He]2S^{(0.47)}2p^{(1.73)}$	$[He]2S^{(0.47)}2p^{(1.69)}3p^{(0.01)}$
	Beta	$[He]2S^{(0.28)}2p^{(0.88)}$	$[He]2S^{(0.47)}2p^{(1.66)}3p^{(0.01)}$	$[He]2S^{(0.47)}2p^{(1.62)}$	$[He]2S^{(0.47)}2p^{(1.68)}3p^{(0.01)}$
X = N	Alpha	$[He]2S^{(0.58)}2p^{(2.12)}$	$[He]2S^{(0.41)}2p^{(1.49)}3p^{(0.01)}$	$[He]2S^{(0.41)}2p^{(1.55)}3p^{(0.01)}$	$[He]2S^{(0.40)}2p^{(1.47)}3p^{(0.01)}$
	Beta	$[He]2S^{(0.58)}2p^{(2.05)}$	$[He]2S^{(0.41)}2p^{(1.46)}3p^{(0.01)}$	$[He]2S^{(0.40)}2p^{(1.41)}3p^{(0.01)}$	$[He]2S^{(0.40)}2p^{(1.48)}3p^{(0.01)}$
X = Al	Alpha	$[Ne]3S^{(0.31)}3p^{(0.40)}$	$[He]2S^{(0.52)}2p^{(1.78)}3p^{(0.01)}$	$[He]2S^{(0.52)}2p^{(1.80)}3p^{(0.01)}$	$[He]2S^{(0.52)}2p^{(1.74)}3p^{(0.01)}$
	Beta	$[Ne]3S^{(0.30)}3p^{(0.36)}$	$[He]2S^{(0.52)}2p^{(1.70)}3p^{(0.01)}$	$[He]2S^{(0.51)}2p^{(1.67)}3p^{(0.01)}$	$[He]2S^{(0.52)}2p^{(1.74)}3p^{(0.01)}$
X = Si	–	$[Ne]3S^{(0.90)}3p^{(1.68)}3d^{(0.02)}4p^{(0.01)}$	$[He]2S^{(1.00)}2p^{(3.45)}3p^{(0.01)}$	$[He]2S^{(0.99)}2p^{(3.43)}3p^{(0.01)}$	$[He]2S^{(0.99)}2p^{(3.45)}3p^{(0.01)}$
X = P	Alpha	$[Ne]3S^{(0.70)}3p^{(1.30)}3d^{(0.01)}4p^{(0.01)}$	$[He]2S^{(0.48)}2p^{(1.73)}3p^{(0.01)}$	$[He]2S^{(0.48)}2p^{(1.77)}3p^{(0.01)}$	$[He]2S^{(0.48)}2p^{(1.69)}3p^{(0.01)}$
	Beta	$[Ne]3S^{(0.67)}3p^{(1.27)}3d^{(0.01)}4p^{(0.01)}$	$[He]2S^{(0.47)}2p^{(1.61)}3p^{(0.01)}$	$[He]2S^{(0.46)}2p^{(1.56)}3p^{(0.01)}$	$[He]2S^{(0.47)}2p^{(1.65)}3p^{(0.01)}$
X = Co	Alpha	$[Ar]4S^{(0.20)}3d^{(3.89)}4p^{(013)}$	$[He]2S^{(0.50)}2p^{(1.61)}3p^{(0.01)}$	$[He]2S^{(0.50)}2p^{(1.66)}3p^{(0.01)}$	$[He]2S^{(0.50)}2p^{(1.57)}3p^{(0.01)}$
	Beta	$[Ar]4S^{(0.17)}3d^{(3.81)}4p^{(0.09)}$	$[He]2S^{(0.50)}2p^{(1.52)}3p^{(0.01)}$	$[He]2S^{(0.49)}2p^{(1.50)}3p^{(0.01)}$	$[He]2S^{(0.50)}2p^{(1.56)}3p^{(0.01)}$
X = Ni	–	$[Ar]4S^{(0.38)}3d^{(8.53)}4p^{(0.31)}$	$[He]2S^{(1.04)}2p^{(3.11)}3p^{(0.02)}$	$[He]2S^{(0.97)}2p^{(3.22)}3p^{(0.02)}$	$[He]2S^{(0.98)}2p^{(3.12)}3p^{(0.02)}$

The contour map of the electron density Laplacian of X—C_{24}-—C_{41} is shown in Fig. 3. The bonded charge concentration (BCC) characterizes a covalent interaction between two atoms when valence electrons are concentrated. The interaction of BCC with the N—C bonds is strong. Therefore, the N—C bonds are highly covalent and have significant negative Laplacians. The Al—C bonds are highly ionic and have significant positive Laplacians. The electron density descriptors of X—C_{24}—C_{22} and X—C_{22}—C_{41} are identical.

The electron localization function (ELF) analysis can provide useful information about chemical bonds. The ELF analyses have been performed to obtain further information about the properties of bonds interactions. The ELF has a range of values between 0 and 1. As the ELF value increases, the electrons are more localized and the nature of an atomic bond will gradually be transformed into a covalent type. The two dimensional coloured ELF images of $C_{79}H_{20}X$ systems are given in Fig. 4. The ELF values of C—B and C—N bonds in $C_{79}H_{20}B$ and $C_{79}H_{20}N$ are close to 0.4. Fig. 4 suggests intuitively that the ELF value of C and X decreases when X changes from B or N to Al, Si or P. The ELF analysis reveals the decrease in covalency of the N—C bond

compared with the Al—C bond and such a decrease is in agreement with the electron density analysis.

3.4. NBO analysis

The natural electronic configurations of X—C_{22}, X—C_{24} and X—C_{41} bonds are listed in Table 3. Most of the valence electrons of the carbon atoms reside in the 2p shell and the least valence electrons occupy the 2s shell. Moreover, there are significant differences between alpha and beta electrons of $C_{79}H_{20}B$, $C_{79}H_{20}N$, $C_{79}H_{20}Al$, $C_{79}H_{20}P$ and $C_{79}H_{20}Co$ regarding the 2p shell population occupancies. The electronic configurations of C_{22}, C_{24} and C_{41} clearly show that the number of electrons occupying the 2s shells of these atoms are very close to each other. Our results show that the $C_{79}H_{20}N$ has the lowest number of electrons in the 2p shells of C_{22}, C_{24} and C_{41} atoms.

The electronic configuration of dopant X atom shows that the valence electrons mainly reside in the ns and np shells (n = 2 for B and N and n = 3 for Al, Si, and P). The number of electrons in the ns and np shells increases when moving from left to right across a period in the periodic table of elements. The number of
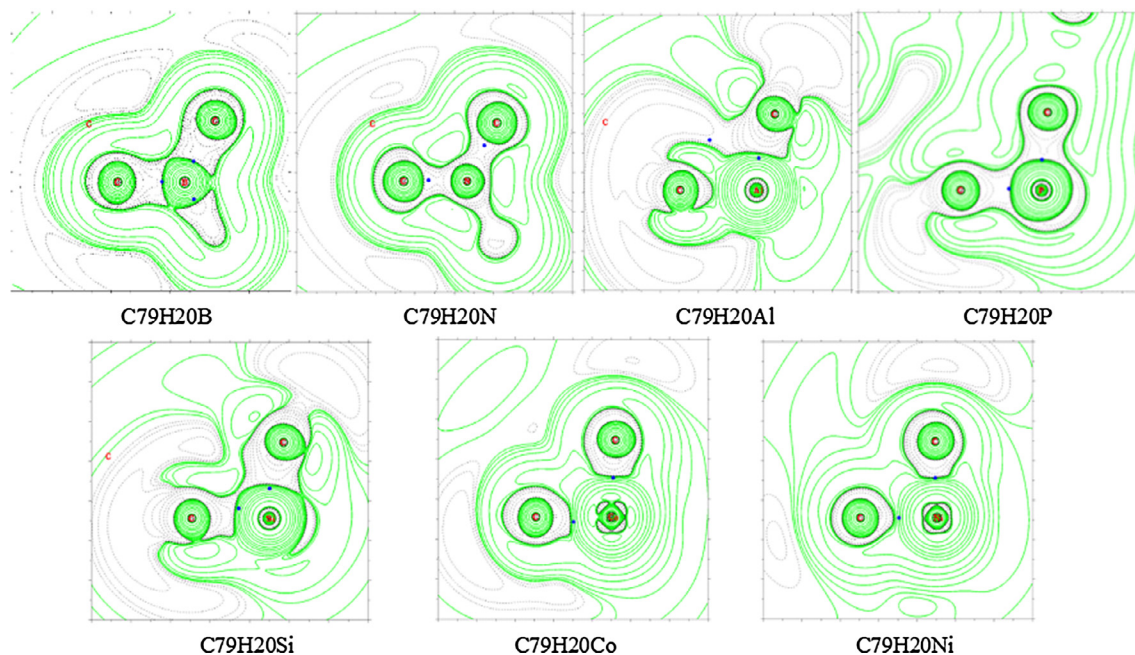
Fig. 3. Contour map of $\nabla^2 \rho(r)$ of geometrically optimized X—C_{24}—C_{41} (geometry optimization by 6-31+G). Solid and dashed lines correspond to positive and negative regions of $\nabla^2 \rho(r)$ respectively. Blue points correspond to bond critical points. (For interpretation of the references to colour in this figure legend, the reader is referred to the web version of this article.)

the ns shell electrons increases when moving from top to bottom in a group of the periodic table, whereas the number of the p shell electrons decreases for the same group move. Thus, the number of electrons in the ns shells of P, N, Si, Al and B and the np shells of N, P, Si, B and Al are said to be in ascending orders and may be denoted as: P > N > Si > Al > B and N > P > Si > B > Al. The valence electrons of Co and Ni atoms reside in the 4s, 4p and 3d shells. In addition, the number of electrons in the 4s shell of Co and Ni atoms are very close to each other and most of the valence electrons reside in the 3d shell. The NBO data calculated by all of our methods and basis sets gave identical results.

In order to characterize the X—C bonds in X-doped nanotubes, the bond lengths, LBO, MBO and FBO were calculated (See Table 4). There are very small differences between the X—C_{22}, X—C_{24} and X—C_{41} bond lengths. These small differences lie in the range of 0.025–0.076 Å. Shorter X—C bonds have larger bond orders. However, X—C_{24} bond is slightly weaker than X—C_{22} and X—C_{41} bonds because its length is longer and has a smaller LBO value. Table 4 shows that the values of LBO differ significantly from the MBO and FBO. The LBO, MBO and FBO ranges of X—C_{22}, X—C_{24} and X—C_{41} bonds are 0.424–1.172, 0.339–1.791 and 1.011–1.297 respectively, indicating that the X atom forms single bond with C atom (See Tables 4 and S4). The N—C has the shortest bond length whereas Al—C has the longest bond length. This phenomenon is in agreement with the electron density analysis. The P—C has a much longer bond length than the N—C and the B—C has a much shorter bond length than Al—C. Therefore, bond length increases when moving from top to bottom in a group of the periodic table. The bond length is determined by bond order. A higher bond order leads to a shorter bond length and a shorter bond length is associated with a stronger bond strength. Thus in a group with increasing bond strength, bond orders of that group elements should be reduced. Table 4 indicates that the LBO has a strong correlation with the bond length. The LBO values of Co—C and Ni—C bonds are reasonable because they are in sensible agreement with their bond lengths.

The charges which were calculated by NPA (Alpha and Beta), Hirshfeld and ADCH methods, are listed in Table S4. Charge

concentration or depletion on the X and the C atoms can be determined by NPA, Hirshfeld and ADCH methods. It can be seen that charge concentrations on the Al and N atoms, calculated by Hirshfeld, are highest and lowest respectively. The charges on N atom, calculated by NPA and ADCH, are negative and the reason for these being negative could be that nitrogen is more electronegative than the other atoms in the $C_{79}H_{20}Xs$. In addition, the atomic charges on all C atoms, except in the $C_{79}H_{20}N$, are negative. Charge negativity is expected owing to the fact that electronegativity of C atom is higher than dopant atoms. The positive charges on the dopant X atom increases when moving from top to bottom in a group of the period table and decreases when moving from left to right across a period. The molecular electrostatic potential (MEP) maps are essential in studying and predicting the reactive sites for electrophilic and nucleophilic attacks. The MEP maps were evaluated at the B3LYP/6-31G(d) level for two directions and are shown in Fig. 5. Fig. 5 also shows MEP ranges on vdW surface. The positive regions of MEP map, shown in green colour, are related to nucleophilic reactivity and the negative regions, shown in blue colour, are associated with electrophilic reactivity. The vdW surface areas of the $C_{79}H_{20}Xs$ are as follows:

Doped SWNT	vdW surface area of MEP map negative region (square Å)	vdW surface area as % of the overall surface of the doped SWNT
$C_{79}H_{20}B$	431.26	64.85%
$C_{79}H_{20}N$	447.97	67.45%
$C_{79}H_{20}Al$	418.04	67.14%
$C_{79}H_{20}Si$	384.05	64.69%
$C_{79}H_{20}P$	447.01	66.61%
$C_{79}H_{20}Co$	420.78	62.63%
$C_{79}H_{20}Ni$	439.56	65.65%

Thus the electrostatic potential distribution of the positive regions of MEP covers a much smaller domain than the negative regions for all the compounds we have studied in this work. The graphs
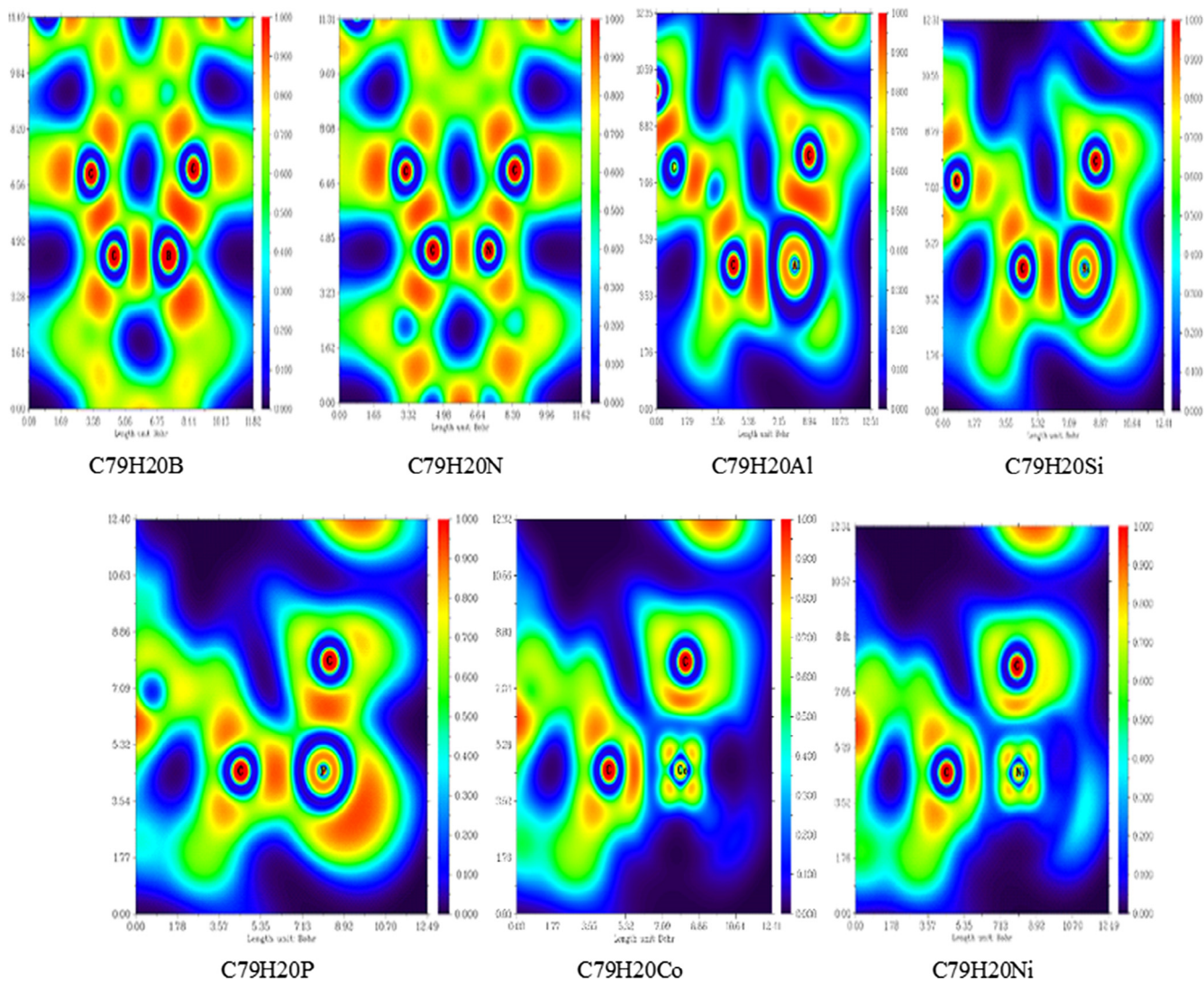
Fig. 4. ELF plots of optimized X-C_{24}-C_{41} (Geometry optimization by B3LYP/6-31+G).

of $C_{79}H_{20}X$ surfaces show that the MEP map of negative region mainly arises from the negative charged carbon atoms and the abundant π-electron cloud. The small areas of the MEP maps have considerable negative ESP and are locations of the global surface minima. The ESP of the $C_{79}H_{20}Xs$ are as follows:

Doped SWNT	ESP (kcal/mol)
$C_{79}H_{20}B$	−19.83
$C_{79}H_{20}N$	−13.48
$C_{79}H_{20}Al$	−16.53
$C_{79}H_{20}Si$	−12.75
$C_{79}H_{20}P$	−20.12
$C_{79}H_{20}Co$	−11.72
$C_{79}H_{20}Ni$	−17.27

The maximum positive regions of $C_{79}H_{20}B$, $C_{79}H_{20}N$, $C_{79}H_{20}Si$ and $C_{79}H_{20}P$ are localized on hydrogen atoms whereas the maximum positive charges of $C_{79}H_{20}Al$, $C_{79}H_{20}Co$, $C_{79}H_{20}Ni$ are mainly concentrated on Al, Co and Ni atoms. In order to compare ESP with NPA, Hirshfeld and ADCH, graphical representation of the ESP with respect to the atomic numbering scheme are shown in Fig. S3.

3.4.1. $C_{79}H_{20}B$

Fig. S3 shows the NPA positive charges on the B atom of the $C_{79}H_{20}B$ are high. The Hirshfeld quasi-charges on the B atom are negative but the Hirshfeld charges on the H atom are positive. The ADCH positive charges on the H atom are high. MEP map of $C_{79}H_{20}B$ indicates that all H atoms are located in the green regions. The electronegativity of C atom is slightly greater than B atom and hence negative charges are delocalized on the C atoms, especially on the C atom which is bonded to the B atom. The NPA and Hirshfeld charges on C_{41}, C_{24} and C_{22} atoms are high, negative and almost equal. The ADCH charge on C_{24} atom is greater than its charge on C_{41} and C_{22} atoms. Fig. 5 shows that the highest negative ESP, which is also the global surface minimum of $C_{79}H_{20}B$, is −19.83 kcal/mol and the most intensive electric field is located close to B atom. The ESPs of $C_{79}H_{20}B$ are in good agreement with ADCH values.

3.4.2. $C_{79}H_{20}N$

Fig. S3 shows that the NPA charge on the N atom of the $C_{79}H_{20}N$ is high and negative but the Hirshfeld charge on the N atom is low and positive. The ADCH charge on the N atom is negative and the highest ADCH negative charges are located on C atoms other than C_{41}, C_{24}, and C_{22} atoms. The NPA, Hirshfeld and ADCH charges on

Table 4
Laplacian bond order (LBO), Mayer bond order (MBO), Fuzzy bond order (FBO), bond distance (Å) of X—C calculated by the B3LYP/6-31G(d).

X	Level	LBO			MBO			FBO			Bond Length		
		X-C41	X-C24	X-C22	X-C41	X-C24	X-C22	X-C41	X-C24	X-C22	X-C41	X-C24	X-C22
X = B	B3LYP/6-31G(d)	1.172	1.101	1.171	1.056	1.076	1.058	1.037	1.052	1.034	1.513	1.518	1.516
	M06-2X/6-31G(d)	1.156	1.084	1.157	1.029	1.049	1.028	1.029	1.049	1.028			
	M06-2X/SDD	0.986	0.921	0.985	1.071	1.041	1.092	1.032	1.050	1.031			
X = N	B3LYP/6-31G(d)	0.866	0.827	0.847	0.923	0.949	0.928	1.173	1.177	1.163	1.409	1.412	1.414
	M06-2X/6-31G(d)	0.852	0.812	0.833	0.914	0.937	0.920	1.171	1.182	1.164			
	M06-2X/SDD	0.586	0.551	0.569	0.985	1.108	0.969	1.159	1.173	1.152			
X = Al	B3LYP/6-31G(d)	0.871	0.748	0.874	1.004	0.993	1.008	1.039	1.055	1.044	1.855	1.877	1.858
	M06-2X/6-31G(d)	0.867	0.748	0.871	0.977	0.977	0.986	1.033	1.053	1.041			
	M06-2X/SDD	0.752	0.637	0.751	0.697	0.782	0.711	1.027	1.047	1.035			
X = Si	B3LYP/6-31G(d)	1.119	1.017	1.157	1.028	1.079	1.115	1.145	1.181	1.209	1.809	1.781	1.789
	M06-2X/6-31G(d)	1.104	1.003	1.141	1.020	1.099	1.128	1.139	1.197	1.219			
	M06-2X/SDD	0.896	0.810	0.929	0.894	0.982	1.006	1.135	1.195	1.216			
X = P	B3LYP/6-31G(d)	0.997	0.862	0.985	0.927	0.015	0.934	1.114	1.074	1.119	1.800	1.834	1.804
	M06-2X/6-31G(d)	0.989	0.856	0.977	0.925	0.878	0.933	1.111	1.077	1.118			
	M06-2X/SDD	0.763	0.657	0.751	0.804	0.842	0.831	1.099	1.066	1.106			
X = Co	B3LYP/6-31G(d)	0.799	0.737	0.803	1.176	1.142	1.188	1.245	1.194	1.266	1.776	1.816	1.773
	M06-2X/6-31G(d)	0.856	0.801	0.860	1.103	1.071	1.121	1.215	1.176	1.235			
	M06-2X/SDD	0.739	0.706	0.734	1.051	0.969	1.072	1.206	1.168	1.225			
X = Ni	B3LYP/6-31G(d)	0.606	0.528	0.614	1.140	0.996	1.252	1.184	1.044	1.297	1.778	1.848	1.778
	M06-2X/6-31 G(d)	0.623	0.531	0.591	1.092	0.957	1.246	1.163	1.047	1.289			
	M06-2X/SDD	0.543	0.491	0.537	1.034	0.847	1.254	1.148	1.029	1.262			

Energies were obtained after 6-31G(d) geometry optimization.

all H, C_{41}, C_{24}, and C_{22} atoms are positive. The ADCH charge is more concentrated on C_{24} atom than on C_{22} and C_{41} atoms but NPA and Hirshfeld charges on C_{41}, C_{24}, and C_{22} atoms are almost equal. Our results show that ADCH method provides a better means of estimating atomic charges of $C_{79}H_{20}N$ molecule. The maximum positive charge is concentrated on H atoms. The NPA, Hirshfeld and ADCH charges on the C atom, which is bonded to the N atom, are positive because the electronegativity of N atom is larger than the C atom, (See Fig. 5).

3.4.3. $C_{79}H_{20}Al$

Fig. 5 illustrates the fact that Al atom in $C_{79}H_{20}Al$ molecule is the site where maximum charge is concentrated and the ADCH, Hirshfeld and NPA charges on the Al atom are positive and greater than the charges on other atoms. The electrostatic potential of $C_{79}H_{20}Al$ indicates that the C atom, which is bonded to the Al atom, provide the site where maximum negative charges is concentrated. The small area of the MEP map has a considerable negative ESP (−16.53 kcal/mol) which stems from the prominent negative charge of C_{24}. The NPA and Hirshfeld data are in good agreement with ADCH values. The NPA, Hirshfeld and ADCH charges on C_{41}, C_{24}, and C_{22} atoms are negative. The ADCH charges on C_{24} atom are greater than the charges on C_{22} and C_{41} atoms but the NPA and Hirshfeld charges on C_{41}, C_{24}, and C_{22} atoms are almost equal.

3.4.4. $C_{79}H_{20}Si$

Fig. S3 shows that the NPA, Hirshfeld and ADCH positive charges on Si atom in $C_{79}H_{20}Si$ are greater than the charges on H atoms. MEP shows that the positive charges on H atoms are highest because the H atoms are in vicinity of positively charged Si atom (See Fig. 5). In addition, the NPA and Hirshfeld charges on C_{41}, C_{24}, and C_{22} atoms are negative and greater than the charges on other C atoms of $C_{79}H_{20}S$. The ADCH quasi-charges on C_{41}, C_{24}, and C_{22} atoms are smaller than the charges on other C atoms and match electrostatic potential of $C_{79}H_{20}Si$.

3.4.5. $C_{79}H_{20}P$

The positive charge on P in $C_{79}H_{20}P$ mainly arises from the positively charged H atoms. The NPA and Hirshfeld positive charges on P are high but the ADCH positive charge on P atom is low. The NPA, Hirshfeld and ADCH charges on C_{41}, C_{24}, and C_{22} atoms are negative. The NPA and Hirshfeld charges on C_{41}, C_{24}, and C_{22} atoms are almost equal. The ADCH charge on C_{24} is greater than the charges on C_{22} and C_{41}. The ESP of $C_{79}H_{20}P$ (−11.03 kcal/mol) stems from the prominent negative charge on C_{24}. The ADCH values are in good agreement ESP of $C_{79}H_{20}P$.

3.4.6. $C_{79}H_{20}Co$

Fig. 5 shows that the maximum positive region of $C_{79}H_{20}Co$ is localized on Co atom and the maximum negative charge is concentrated on the C atom close to the Co atom. The reason that the maximum negative charge is concentrated on C atom is the effect of high electronegativity of Co atom. The small areas of MEP map (0.04%), which have considerable positive ESP (32.39 kcal/mol), correspond to the regions closed to the global ESP maximum. The maximum positive site occupies 37.37% of the overall surface. The NPA, Hirshfeld and ADCH positive charges on Co atom are high. The NPA, Hirshfeld and ADCH negative charges on C_{41}, C_{24}, and C_{22} atoms are greater than the charges on other C atoms. The NPA, Hirshfeld and ADCH charges on C_{24} are greater than the charges on C_{22} and C_{41}.

3.4.7. $C_{79}H_{20}Ni$

The maximum negative charge is concentrated on the C atom bonded to the Ni atom and the maximum positive region is localized on Ni atom. The positive charge on Ni atom is higher than the charges on other atoms. The NPA, Hirshfeld and ADCH negative charges on C_{41}, C_{24}, and C_{22} atoms are highest. The Hirshfeld and NPA charges on C_{24} are greater than the charges on C_{22} and C_{41}. The ADCH charge on C_{22} is greater than the charges on C_{24} and C_{41}.
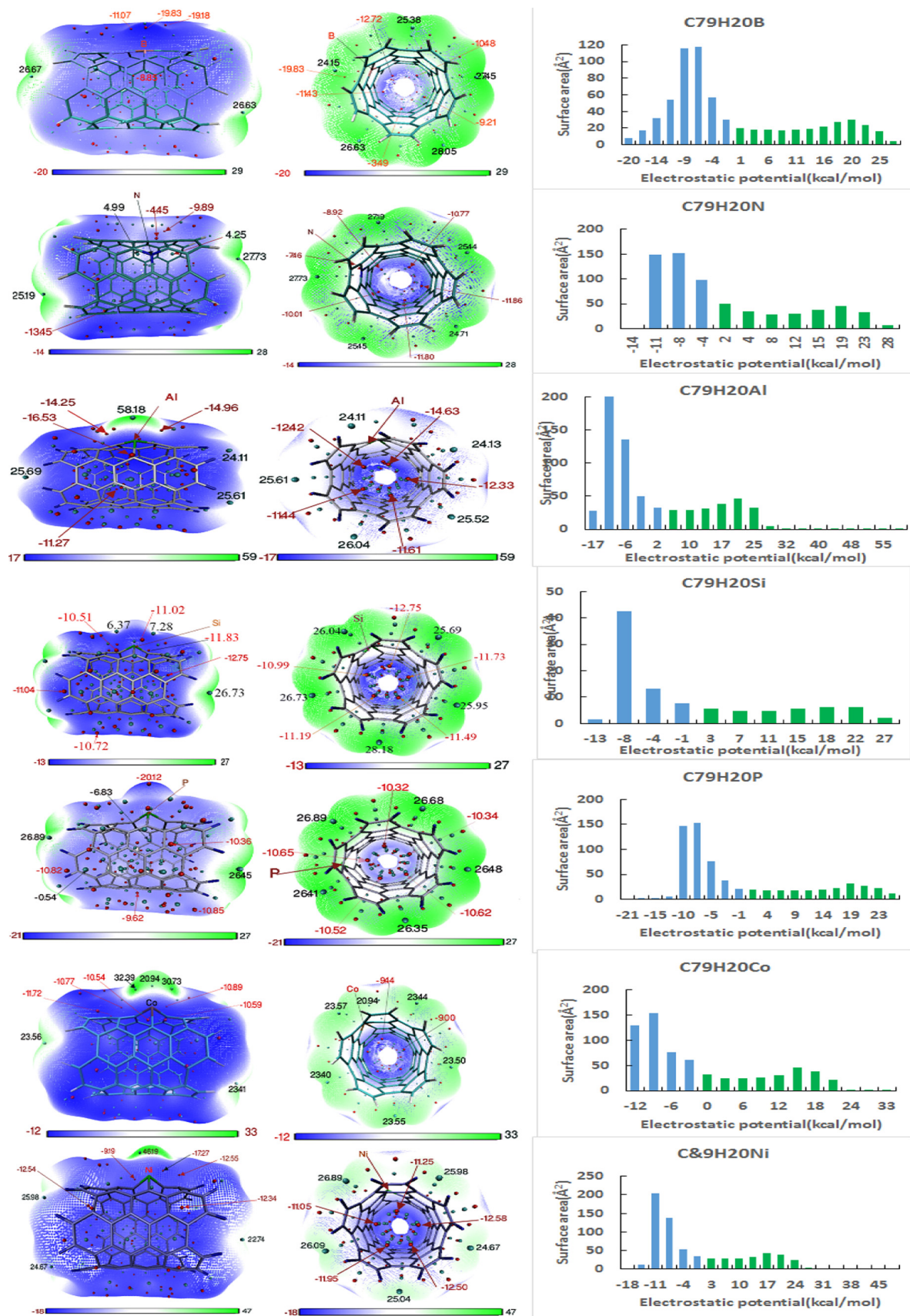
Fig. 5. Electrostatic potential on vdW surfaces (the units are in kcal/mol) of $C_{79}H_{20}X$ (X = B, N, Al, Si, P, Co, Ni) calculated at the B3LYP/6-31+G level.

4. Conclusions

Computational chemistry simulations were carried out for $C_{79}H_{20}Xs$.

The energy gaps of $C_{79}H_{20}Xs$, calculated by B3LYP/6-31G(d) method, are greater than those calculated by B3LYP/6-31+G method but are much smaller than the energy gaps that were obtained by M06-2X density functional method using 6-31+G, 6-31G(d) and SDD basis sets. The energy gaps of the $C_{79}H_{20}Xs$ are greater than those of pristine $C_{80}H_{20}$ nanotube. The $C_{80}H_{20}$ nanotube keeps its metallic property after being doped with impurities. The DOS trends of $C_{79}H_{20}Xs$ are similar to the trends of their energy gaps.

The topological analysis shows that the X—C bonds in $C_{79}H_{20}Xs$ are single type and the nature of the interaction between C and the X atoms is not purely covalent or ionic. The N—C bond of $C_{79}H_{20}N$ is highly covalent and have significant negative Laplacians whereas the Al—C bond of $C_{79}H_{20}Al$ is highly ionic and have significant positive Laplacians. The ELF analysis and contour map of electron density of $C_{79}H_{20}Xs$ confirms the high covalency and ionocity of the N—C and the Al—C bonds respectively.

The N—C has the shortest bond length and Al—C has the longest bond length. LBO has a strong correlation with the bond length in comparison with MBO and FBO. The NPA, Hirshfeld and ADCH atomic charges and molecular electrostatic potential maps on vdW surfaces of $C_{79}H_{20}Xs$ show that ESP values are in good agreement with ADCH values.

Calculations of natural bond orbital (NBO) analysis, bond order analysis, atomic charge analysis, and electrostatic potential on the van der Waals (vdW) surfaces of $C_{79}H_{20}Xs$ were carried out and we gained a deeper understanding of the interaction between X atoms and C atoms in $C_{79}H_{20}Xs$. This work presents a comparison about the bonding characteristic between the doped atoms (X) and carbon atoms. These results can provide detailed information on the bonding principles of the X—C bonds.

Acknowledgments

Appendix A. Supplementary material

Supplementary data associated with this article can be found, in the online version, at http://dx.doi.org/10.1016/j.comptc.2017.05.016.

References

[1] S. Iijima, Nature 354 (1991) 56–58.
[2] R. Saito, M. Fujita, G. Dresselhaus, M.S. Dresselhaus, Phys. Rev. B 46 (1992) 1804.
[3] N. Hamada, S.-I. Sawada, A. Oshiyama, Phys. Rev. Lett. 68 (1992) 1579.
[4] M. Dresselhaus, G. Dresselhaus, R. Saito, Carbon 33 (1995) 883–891.
[5] C.M. Lieber, Solid State Commun. 107 (1998) 607–616.
[6] R.E. Smalley, B.I. Yakobson, Solid State Commun. 107 (1998) 597–606.
[7] T.W. Odom, J.-L. Huang, P. Kim, C.M. Lieber, Nature 391 (1998) 62–64.
[8] B. Babic, J. Furer, S. Sahoo, S. Farhangfar, C. Schönenberger, Nano Lett. 3 (2003) 1577–1580.
[9] D. Sánchez-Portal, E. Artacho, J.M. Soler, A. Rubio, P. Ordejón, Phys. Rev. B 59 (1999) 12678.
[10] V. Popov, V. Van Doren, M. Balkanski, Phys. Rev. B 61 (2000) 3078.
[11] S.J. Tans, A.R. Verschueren, C. Dekker, Nature 393 (1998) 49–52.
[12] J. Cao, Q. Wang, H. Dai, Phys. Rev. Lett. 90 (2003) 157601.
[13] R.J. Grow, Q. Wang, J. Cao, D. Wang, H. Dai, Appl. Phys. Lett. 86 (2005) 093104.
[14] P.G. Collins, K. Bradley, M. Ishigami, A. Zettl, Science 287 (2000) 1801–1804.
[15] J. Kong, N.R. Franklin, C. Zhou, M.G. Chapline, S. Peng, K. Cho, H. Dai, Science 287 (2000) 622–625.
[16] X. Feng, S. Irle, H. Witek, K. Morokuma, R. Vidic, E. Borguet, J. Am. Chem. Soc. 127 (2005) 10533–10538.
[17] J. Li, Y. Lu, Q. Ye, M. Cinke, J. Han, M. Meyyappan, Nano Lett. 3 (2003) 929–933.
[18] A. Goldoni, R. Larciprete, L. Petaccia, S. Lizzit, J. Am. Chem. Soc. 125 (2003) 11329–11333.
[19] R.J. Chen, H.C. Choi, S. Bangsaruntip, E. Yenilmez, X. Tang, Q. Wang, Y.-L. Chang, H. Dai, J. Am. Chem. Soc. 126 (2004) 1563–1568.
[20] R.J. Chen, Y. Zhang, D. Wang, H. Dai, J. Am. Chem. Soc. 123 (2001) 3838–3839.
[21] A. Bianco, K. Kostarelos, M. Prato, Curr. Opin. Chem. Biol. 9 (2005) 674–679.
[22] N.W.S. Kam, Z. Liu, H. Dai, J. Am. Chem. Soc. 127 (2005) 12492–12493.
[23] R. Bian, J. Zhao, H. Fu, J. Mol. Model. 19 (2013) 1667–1675.
[24] S. Peng, K. Cho, Nano Lett. 3 (2003) 513–517.
[25] S.B. Fagan, A. Souza Filho, J. Lima, J.M. Filho, O. Ferreira, I. Mazali, O. Alves, M. Dresselhaus, Nano Lett. 4 (2004) 1285–1288.
[26] Y. Zhang, Y. Zhang, D. Zhang, C. Liu, J. Phys. Chem. B 110 (2006) 4671–4674.
[27] J.A. Talla, Phys. B: Condens. Matter 407 (2012) 966–970.
[28] J.-J. Adjizian, R. Leghrib, A.A. Koos, I. Suarez-Martinez, A. Crossley, P. Wagner, N. Grobert, E. Llobet, C.P. Ewels, Carbon 66 (2014) 662–673.
[29] R. Wang, D. Zhang, Y. Zhang, C. Liu, J. Phys. Chem. B 110 (2006) 18267–18271.
[30] T. Koretsune, S. Saito, Phys. Rev. B 77 (2008) 165417.
[31] M.T. Baei, Fullerenes, Nanotubes Carbon Nanostruct. 20 (2012) 681–687.
[32] R. Wang, D. Zhang, W. Sun, Z. Han, C. Liu, J. Mol. Struct.: THEOCHEM 806 (2007) 93–97.
[33] Q. Zhao, M. Buongiorno Nardelli, W. Lu, J. Bernholc, Nano Lett. 5 (2005) 847–851.
[34] P. Gowrisankar, K. Udhayakumar, J. Nanomater. 2013 (2013) 149.
[35] Y. Hizhnyi, S.G. Nedilko, V. Borysiuk, V.A. Gubanov, Int. J. Quant. Chem. 115 (2015) 1475–1482.
[36] A.D. Becke, J. Chem. Phys. 98 (1993) 5648–5652.
[37] M. Frisch, G. Trucks, H. Schlegel, G. Scuseria, M. Robb, J. Cheeseman, G. Scalmani, V. Barone, B. Mennucci, G. Petersson, Phys. Rev. B: Condens. Matter Mater. Phys 37 (1988) 785.
[38] S. Manzetti, T. Lu, RSC Adv. 3 (2013) 25881–25890.
[39] G. Abadir, K. Walus, D. Pulfrey, J. Computat. Electron. 8 (2009) 1–9.
[40] Y. Zhao, D.G. Truhlar, Theor. Chem. Acc. 120 (2008) 215–241.
[41] L.A. Burns, Á. Vázquez-Mayagoitia, B.G. Sumpter, C.D. Sherrill, J. Chem. Phys. 134 (2011) 084107.
[42] P.J. Hay, W.R. Wadt, J. Chem. Phys. 82 (1985) 270–283.
[43] J. Zhao, Y. Zhang, L. Zhu, J. Mol. Struct.: THEOCHEM 671 (2004) 179–187.
[44] T. Lu, F. Chen, J. Computat. Chem. 33 (2012) 580–592.
[45] A.E. Reed, R.B. Weinstock, F. Weinhold, J. Chem. Phys. 83 (1985) 735–746.
[46] T. Lu, F. Chen, J. Theor. Computat. Chem. 11 (2012) 163–183.
[47] T. Lu, F. Chen, J. Phys. Chem. A 117 (2013) 3100–3108.
[48] I. Mayer, Chem. Phys. Lett. 97 (1983) 270–274.
[49] I. Mayer, P. Salvador, Chem. Phys. Lett. 383 (2004) 368–375.
[50] T. Lu, F.-W. Chen, Acta Phys.-Chim. Sin. 27 (2011) 2786–2792.
[51] W. Humphrey, A. Dalke, K. Schulten, J. Mol. Graphics 14 (1996) 33–38.
[52] Z. Zhou, M. Steigerwald, M. Hybertsen, L. Brus, R.A. Friesner, J. Am. Chem. Soc. 126 (2004) 3597–3607.
[53] N.L. Marana, S. Casassa, E. Longo, J.R. Sambrano, J. Phys. Chem. C 120 (2016) 6814–6823.
[54] Q.-Y. Wu, J.-H. Lan, C.-Z. Wang, Y.-L. Zhao, Z.-F. Chai, W.-Q. Shi, J. Phys. Chem. A 119 (2015) 922–930.
[55] D. Chakraborty, P.K. Chattaraj, J. Phys. Chem. A 119 (2015) 3064–3074.